Intracycle Control Sensitivity of Cross-Flow Turbines

Ari Athair, Abigale Snortland, Isabel Scherl, Brian Polagye, Owen Williams

Abstract—**Intracycle control for cross-flow turbines employs sinusoidal perturbations in rotational speed to affect turbine power output and loads. This technique is explored for one- and two-bladed turbines with experiments that combine performance measurements with in-rotor flow-field measurements using non-intrusive particle image velocimetry. Performance enhancement is demonstrated for a wide range of control parameters but is found to be more sensitive to the sinusoidal phase offset than amplitude. Optimal performance is observed under conditions which maintain constant nominal blade angle of attack and consistently high blade-relative velocities once the static stall angle is exceeded during the power stroke. This maintains high lift and delays vortex separation. Perhaps most significantly, kinematics are also identified which decrease peak turbine loading by 12% while still producing marginally higher power output, highlighting the utility of intracycle control for load mitigation. The range of control parameters that produce these beneficial loading properties is relatively narrow and flow-fields are similar to operation at a constant rotation rate. We hypothesize that reductions in maximum loading are achieved by smoothing the changes in angle of attack and blade relative velocity profiles throughout the cycle.**

Index Terms—**Cross-flow Turbines, Marine Renewable Energy, Flow Control, Hydrokinetic Energy, Variable Velocity Control**

I. Introduction

CROSS-FLOW turbines show promise for various power applications due to constructive interference in arrays, decreased environmental impacts, and acoustic pollution as a result of their low rotation rates, direction agnostic operation, and their rectangular profile [1]. Despite their potential, cross-flow turbines remain poorly understood. Due to large, periodic changes in blade angle of attack, cross-flow turbines experience complex dynamics and unsteady flow separation, making modeling, simulation and design of these turbines challenging [2], [3]. As a result, there are few dependable and generalizable design processes. Many methods have been tested to control the flow over turbine blades and to improve their power output and efficiency. For example, active blade pitching, plasma actuators, jet injection, and profile cutouts along the blades' edges have been explored [4]. However, each of these increases the complexity and often requires power investment to see benefits. Intracycle velocity control, varying the rotation rate of the turbine as a function of position, has been demonstrated to improve efficiency by up to 53% over a turbine operated at a constant rotation rate [5], [6]. These previous studies employed optimization schemes to find improved control kinematics. In this work, we explore the sensitivity of the intracycle control parameter space and its potential to control turbine loading in addition to power output.

Traditionally, cross-flow turbines operate under constant speed or torque control and performance is often characterized as a function of the non-dimensional rotation rate of the turbine, called the tip-speed ratio, $\lambda = \omega R/U_\infty$, where ωR is the tangential velocity of the turbine blade and U_∞ is the free stream velocity [7]. Under the simplest form of intracycle control, the velocity is changed as a function of blade position in a sinusoidal manner. The variable velocity controller explored in this work takes the form,

$$\lambda_{control} = \lambda_0 + A_\lambda cos(N(\theta - \phi)) \quad (1)$$

where λ_0 is the mean tip-speed ratio, A_λ is the amplitude, and ϕ is the phase shift corresponding to the azimuthal position of the blade where the maximum velocity is seen. In this study, azimuthal blade position, θ is defined as zero where the blade is pointed upstream (see Fig. 1). N is the number of blades of the turbine. This control scheme can be achieved without adding additional complexity or cost to the system.

Increased efficiency resulting from intracycle control was empirically found to occur when the peak cycle torque is aligned with the maximum rotation rate, leading to increased power production [5]. These results are corroborated by the computational studies of Dave *et al.* [6], [8], which demonstrated that intracycle control flow-fields see higher relative velocity and delayed leading-edge vortex formation through the power-producing regions of the cycle when compared to constant speed control, prolonging torque generation [8]. In these previous studies, search algorithms such as Nelder-Mead were utilized to converge to kinematics with optimal efficiency. Since the full

This work was supported in part by the U.S. Department of Defense's Navel Facilities Engineering Systems Command (N0002421D6400/N0002421F8712) and the U.S. Department of Energy TEAMER Program

Authors A. A. and O. W. are with the William E. Boeing Department of Aeronautics and Astronautics at the University of Washington, Steven's Way, Box 352400 Seattle, WA 98195 U.S.A. (e-mail: aristone@uw.edu, ojhw@uw.edu respectively).

Authors A. S. and B. P. are with the Department of Mechanical Engineering at the University of Washington, Steven's Way, Box 352600 Seattle, WA 98195 U.S.A. (e-mail: abigales@uw.edu, brianpolayge@uw.edu respectively).

Author I. S. was with the Department of Mechanical Engineering at the University of Washington, Steven's Way, Box 352600 Seattle, WA 98195 U.S.A. They are now with the Department of Mechanical Civil Engineering at California Institute of Technology, 300 Gates-Thomas Laboratory MC 104-44 Pasadena, CA 91125 U.S.A. (e-mail: ischerl@caltech.edu).

Digital Object Identifier:
https://doi.org/10.36688/ewtec-2023-paper-400

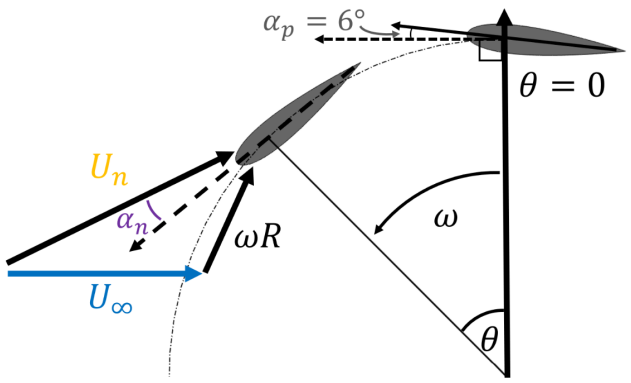

Fig. 1. Nominal blade-level coordinate system and velocities.

range of potential kinematics have not been thoroughly explored, a study of the sensitivities of the amplitude-phase parameter space would yield significant new information with regard to the sensitivity of kinematic optima. In addition, enhancements to power output are often associated with increases in loading, accentuating structural challenges. If other optimization objectives beyond power could be used and kinematics could be uncovered that manage loading while enhancing or maintaining performance, such schemes could significantly impact the cost and management of deployed systems. This information would be invaluable when designing control schemes for operational deployment.

This study aims to experimentally explore the sensitivity of turbine performance to sinusoidal intracycle control parameters and uncover the hydrodynamic sources of these sensitivities. We investigate the impact of sinusoidal intracycle kinematics on power, torque, and loading throughout a large parameter space of intracycle amplitudes and phases for single and double-bladed turbines. The objective is to investigate the possible use of intracycle control to reduce turbine forces while mitigating the impact on power production and tie changes in performance to variations in hydrodynamic features.

II. Methods

A. Cross flow turbine theory

A summary of turbine blade coordinates, and relative velocities are shown in Fig. 1. The nominal relative velocity experienced by the blade U_n and angle of attack α_n calculated from geometry (neglecting induction) were calculated geometrically as,

$$U_n(\theta) = \sqrt{\lambda(\theta)^2 + 2\lambda(\theta)cos(\theta) + 1} \tag{2}$$

$$\alpha_n(\theta) = -tan^{-1}\left[\frac{sin(\theta)}{\lambda(\theta) + cos(\theta)}\right] + \alpha_p \tag{3}$$

and used to provide an approximate understanding of near-blade hydrodynamics.

Torque produced by the fluid-blade interaction of the turbine generates power and is explored in the non-dimensional form,

$$C_Q = \frac{\tau}{\frac{1}{2}\rho A U_\infty^2} \tag{4}$$

the torque coefficient, where ρ is the density, A is turbine projected area, τ is the torque and U_∞ is the inflow velocity far upstream of the turbine. Turbine performance or efficiency is defined in terms of the coefficient of power, or the ratio of mechanical power, $\tau\omega$, to the kinetic power present in the water flowing through the cross-sectional area of the turbine as,

$$C_P = \frac{\tau\omega}{\frac{1}{2}\rho A U_\infty^3}. \tag{5}$$

Similarly, the horizontal force coefficient is defined as a normalized vector sum of the forces perpendicular to the turbine's central shaft,

$$C_F = \frac{F_{XY}}{\frac{1}{2}\rho A U_\infty^2}. \tag{6}$$

In this study, we explore the relative power and loading of the turbine and define the average power-to-peak force ratio (PFR), which describes the amount of power that can be extracted, on average, relative to the maximum loading on the turbine rotor at any point in a cycle. In other words,

$$PFR = \frac{\overline{C_P}}{max(C_F)} = \frac{\overline{\tau\omega}}{max(F_{XY})U_\infty}. \tag{7}$$

Time-averaged metrics are chosen to encompass an integer number of rotations and denoted by an overbar, e.g. $\overline{C_P}$.

B. Test facilities

This work was completed at the University of Washington in the Alice C. Tyler recirculating water flume, which has a 4.6 m long and 0.76 m wide (W) test section, operated with a dynamic depth, H, of 0.56 m. The temperature, depth, and inflow velocity were controlled to maintain consistent non-dimensional parameters such as the blockage, Reynolds, and Froude numbers. The temperature of the water was held at 29 °C using a pool heater. The inflow velocity was 0.885 m/s with a turbulence intensity of between 2-3% [9], as measured five diameters upstream of the turbine position by an acoustic Doppler velocimeter (ADV), Nortek Vectrino. The ADV data collection occurred at a sample rate of 16 Hz and is assumed to be free of turbine induction effects.

C. Turbines

Two turbine configurations were employed; one for performance measurement and another for flow-field particle image velocimetry (PIV) acquisition. Both turbines could be operated in single- or double-bladed configurations. These blades were NACA 0018 aerofoils with a chord, c, of 4.06 cm and span, s, 23.4 cm, and were mounted at a preset pitch, α_p, of 6° rotated outwards about the quarter chord. A 1.27 cm diameter central shaft supported both configurations. The turbine diameter, D, was 17.2cm for a chord-to-radius ratio of 0.47 and chord-based Reynolds number, $Re_c = cU_\infty/\nu$, of 44×10^3. The Froude number, $Fr = U_\infty/\sqrt{gH}$, was 0.38 and the turbine blockage

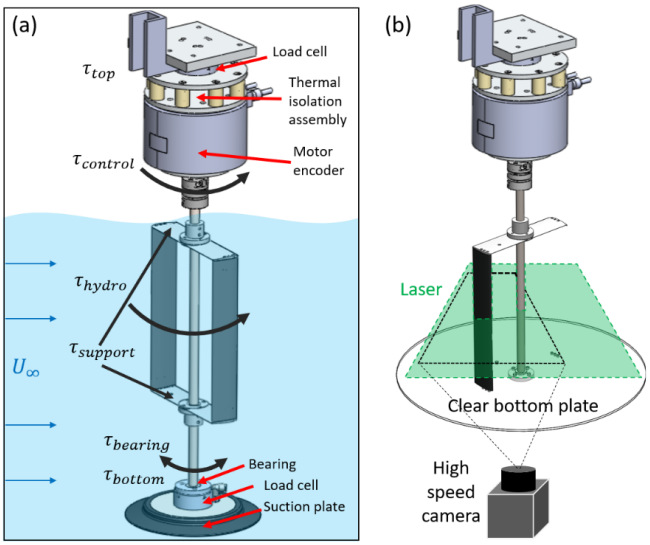

Fig. 2. (a) Experimental configuration used to collect force and performance data. (b) Cantilevered experimental setup used to capture in rotor PIV.

ratio, $\beta = sD/HW$, was 9.5%. The turbine solidity was $\sigma = Nc/\pi D$ of 0.15 for the two-bladed turbine and σ of 0.08 for the single-bladed turbine.

The performance turbine was a pinned configuration (shown in Fig. 2a), employing a suction plate on the bottom of the flume. The blades were fastened to the central shaft by two thin ~NACA 0008 profile strut-type endplates to reduce drag. Two ATI six-axis load cells, Mini40 and Mini45, were mounted at the top and bottom of the turbine central shaft, respectively. These load cells measured the moments and forces on the turbine at 1 kHz. A 5 Nm servomotor (Yaskawa SGMCS-05B3C41), equipped with an internal encoder with resolution of 2^{18} counts-per-revolution, rotated the turbine to desired control kinematics and measured the position and velocity throughout the cycle. All turbine performance information was acquired using Matlab Simulink Desktop in Real-time. During operation, data was collected for 45 s for each control scheme, the time found to be necessary to achieve convergence of cycle-to-cycle performance fluctuations. To remove high-frequency motor noise, a low-pass Butterworth filter with a pass frequency of 75 Hz and cutoff at 175 Hz was applied to the extracted data. This filter was found to have no impact on time-averaged performance.

A sweep of turbine performance was conducted across a wide range of intracycle phases and amplitudes to obtain a better understanding of the performance space. The position of max velocity ϕ phase shift was varied between 0 and 180° (limited due to the symmetry of a two-bladed turbine). The amplitude of velocity change (A_λ/λ_0) was varied between 0 (constant speed control) and 0.64 (i.e. 64 percent of the mean tip-speed ratio). These two variables were discretized in a 21 × 22 grid resulting in the testing of 462 control kinematics profiles. The single-bladed configuration was tested under two-bladed kinematics.

Torque, forces, and accelerations increase greatly with intracycle control amplitude, leading to potential degradation of the motor controller's ability to track prescribed motion. Controller efficacy was explored by comparing the R-squared metric ($R^2 = 1 - \sum_{i=1}^{n}(y_i - f(x_i))^2 / \sum_{i=1}^{n}(y_i - \overline{y})^2$ where y_i is a value in the sample, $\overline{y}$ is the mean value, and $f(x_i)$ is the measured value of y_i) and root mean squared error (RMSE) calculated using the commanded turbine position and velocity and those recorded by the motor encoder. The R^2 values were found to be greater than 0.9997 until $A_\lambda = 0.56\lambda_0$, after which values gradually dropped to 0.995. The RMSE demonstrated a similar trend and was near zero until the same value of A_λ, after which the RMSE grew rapidly with increasing A_λ, to 0.5 at $A_\lambda = 0.64$. This slight error is a result of the servomotor struggling to match the commanded values, leading to a maximum undershooting of the phase shift by 2.5°, an increase in λ_0 by a maximum 0.02 and a minimal increase in A_λ of 1.5% relative to the commanded values. Despite these small errors, the turbine followed the specified parameters sufficiently closely across the full range of explored values and this analysis informed the maximum amplitudes tested in subsequent experiments.

To analyze blade-level performance the influence of the supports must be estimated and subtracted from the measured full-turbine performance. We apply the principle of superposition, following analysis of Strom *et al.* [5], to account for inertial influences resulting from angular acceleration and deceleration. While intracycle control adds the additional complication of angular acceleration and deceleration, the superposition of blade and support influences to arrive at full turbine performance has been shown to be a good approximation for measurements of torque and forces in a number of studies [10], [11]. Following these studies, auxiliary experiments were conducted to measure the influence of the blade support structure without the blades present, assuming negligible interaction between the blades and supports. As a result, the hydrodynamic torque or efficiency was calculated as,

$$\tau_H(\theta) = \tau_{T,measured}(\theta) + I_T\dot{\omega}(\theta) - (\tau_{S,measured}(\theta) + I_S\dot{\omega}(\theta)) \quad (8)$$

where subscripts H, T, and S correspond to the hydrodynamic (or blade), total turbine, and support-only turbine, respectively. The moment of inertia of the turbine, I, is required to determine phase-averaged blade performance. Assigning an arbitrary acceleration scheme and rotating the turbine in air allowed the moment of inertia to be estimated, assuming negligible drag in air. The moment of inertia for the one- and two-bladed turbines were found to be $I = 7.3 \times 10^{-3}$ kgm^2 and 6.4×10^{-3} kgm^2, respectively. For inertial subtraction, the moment of inertia of the turbine with no blades was $I = 5.5 \times 10^{-3}$ kgm^2.

To calculate time/full-cycle averaged performance, it is not necessary to subtract the inertial effects of the control as these integrate to zero across a single cycle, however, removing the time-averaged influence of the support structure is still necessary. For a two-bladed turbine, the center of mass is located at the

center of the turbine, and inertial effects do not impact turbine forces; however, this is not the case for a one-bladed turbine. As the center of mass of a one-bladed turbine is not located at the shaft, accelerations from intracycle control cause turbine-level horizontal forces. As a result, single-bladed turbine forces were not analyzed due to uncertainty in the turbine center of mass location, which prevented the estimation of hydrodynamic blade forces.

The second turbine configuration was a cantilevered assembly (shown in Fig. 2b) rigidly mounted to the same motor with one strut-type endplate and an acrylic disk support at the bottom of the blades. This configuration allowed the acquisition of in-rotor phase-locked PIV using a high-speed camera beneath the flume; more details can be found in [9]. Controller accuracy was tested for this configuration and found to be similar to that of the pinned performance configuration.

D. PIV measurement

Single camera, two-component PIV was used to capture the in-rotor hydrodynamics following the configuration shown in Fig. 2b. A single Phantom V641 high-speed camera with a 55 mm focal length lens captured images within a plane normal to the blades at their center span. The flow was illuminated by a 30 mJ per pulse Continuum Terra PIV Nd:YLF laser, producing a light sheet approximately 2 mm thick. Two mirrors positioned on the opposite side of the flume were used to reflect the laser sheet back into the rotor to reduce the extent of shadowed regions and improve data yield. Two fields of view (FoV), 15.7×25.1 cm^2 were captured, one positioned to capture the upstream and one the downstream regions of the blade path with an approximate 3 cm overlap. Acquisition phases were chosen to ensure PIV data were acquired at specified blade positions. Within each FoV, 30 equally spaced phases were captured with a 12° phase spacing using a trigger from the MATLAB Simulink turbine controller. At each phase, 85 image pairs were captured. This was done for each chosen kinematic and FoV so that low-noise phase-averaged flow-fields could be reconstructed and analyzed. The inter-frame time was chosen to be 350 μs such that the maximum in-plane displacements were limited to approximately 9 pixels. The image calibration was 10.16 pixels/mm.

PIV data were analyzed using LaVision DaVis 10.2 software employing a multi-grid, multi-pass approach with iterative image deformation. Butterworth high-pass background subtraction was applied as a pre-possessing step to remove background illumination. Hand-drawn masks were made for each phase to remove non-illuminated regions, such as the central shaft and blade shadows. The interrogation window size of the final pass was set to 32×32 pixels with 75% overlap. As a result, there were 12.9 vectors per blade chord. A vector post-processing step was applied three times and employed universal outlier detection to filter spurious vectors in a 5×5 pixel domain with a threshold of 3 standard deviations. The resulting processed data was exported and phase-averaged for further plotting and analysis in MATLAB.

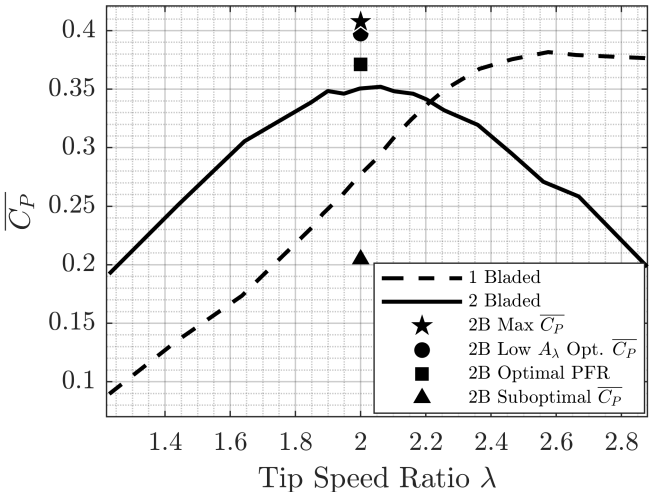

Fig. 3. Support subtracted turbine efficiency under constant speed control of both one and two-bladed turbines. The black symbols represent performance under intracycle kinematics of interest for a two-bladed turbine.

III. Results and Discussion

A. Test conditions

The optimal constant tip speed ratio, λ_0, for a two-bladed turbine under constant speed control was found to be two (see Fig. 3). This tip-speed ratio was selected as the mean for all subsequent intracycle control testing for single and double-bladed configurations. At this tip-speed ratio, the single-bladed turbine has lower performance, as its peak $\overline{C_P}$ occurs closer to λ = 2.5 as a consequence of lower solidity and induction. We expect a single-bladed turbine operating below its optimal tip-speed ratio experiences more significant flow separation and dynamic stall than a two-bladed turbine at the same operating condition.

B. 2-Bladed turbine performance

The two-bladed turbine power coefficient as a function of intracycle phase, ϕ and amplitude, A_λ/λ_0, is visualized in Fig. 4. Consistent with previous studies, significant increases in time-averaged performance are possible under intracycle control. In this case, an increase of up to 14.4% is observed under optimal kinematics, which is found to be alike previous studies that employed a similar turbine geometry at comparable Reynolds numbers. However, the percentage increase in $\overline{C_P}$ compared to constant speed control is lower (53% experimentally by Strom *et al.*, and 54% by Dave *et al.* computationally [5], [8]). Some of this difference is likely attributable to variations in the experimental setup and blade mounting supports, such as the use of disk end plates in earlier studies, the influence of which were not subtracted in the prior experimental work and could lead to a significant amount of drag. The flow speed and non-dimensional parameters are also slightly different between this and previous experimental works. Finally, we note that the percentage change metric is quite sensitive to small changes in the time-averaged constant speed performance of the turbine. These differences are unlikely to explain all of

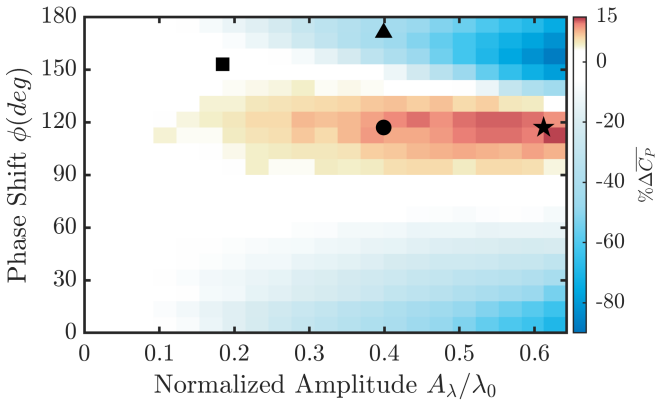

Fig. 4. Percent change in full turbine $\overline{C_P}$ relative to constant speed (λ = 2) control condition for the two-bladed turbine. The colors represent beneficial (red) and detrimental (blue) percent changes to time-averaged $\overline{C_P}$ relative to a constant speed control case, A_λ = 0. The black symbols represent kinematics of interest (star) maximum $\overline{C_P}$, (circle) lower amplitude beneficial $\overline{C_P}$ (triangle) poor performing $\overline{C_P}$ and (square) which corresponds to optimal PFR.

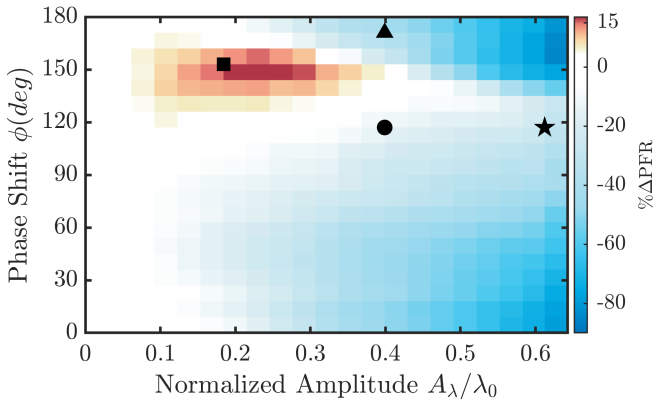

Fig. 5. Percent change in turbine PFR relative to constant speed (λ = 2) control condition for the two-bladed turbine. The colors represent beneficial (red) and detrimental (blue) percent changes to PFR relative to a constant speed control case, A_λ = 0. The black symbols represent the kinematics of interest described in Fig. 4.

the performance amplification between this work and previous studies; however, the kinematics producing optimal performance is very similar between all three studies, suggesting the dynamics are as well.

Fig. 4 also provides an overview of turbine power output sensitivity, in contrast to earlier studies which simply sought a single optimal set of kinematics for maximum power output. Within an approximate 50° range of phase offsets (90 - 140°), the performance is not particularly sensitive to kinematics, and we see a consistent performance improvement with increasing intracycle control amplitude. Not all intracycle kinematics are beneficial, however, and large losses are present for some ϕ values outside this range (up to 90% loss in power is seen for some kinematics). While ϕ appears to have a larger role in controlling differences in performance, changes in amplitude appear to primarily amplify the performance (positive or detrimental) at fixed values of ϕ. This is apparent from the horizontal stratification of the Fig 4. Since the control kinematics are defined as a function of position and the blade spends less time in regions of high rotational velocity, the time-averaged $\overline{\lambda}$ decreases with increasing amplitude of intracycle control. This decrease in $\overline{\lambda}$ may be partially responsible for the performance drop-off at the highest A_λ values.

Increases in power output are often associated with increases in average turbine loading. As a result, we explore the influence of intracycle control on the turbine loading through the PFR (see Fig. 5), given the importance of maximum loads on turbine design. A region where power can be augmented relative to the maximum loading is observed. At the maximum (square), there is a 17.5% improvement in PFR, which can be broken down to a 12% decrease in maximum lateral force and a 3% increase in turbine efficiency. Note that PFR does not consistently increase with turbine intracycle amplitude, as seen for performance. For $A_\lambda/\lambda_0 > 0.35$, the PFR is always less than the constant speed counterpart. Reduced maximum loading also occurs for a slightly lower range of intracycle phase offsets (130 - 160°).

Throughout the remainder of the paper, we choose to highlight two additional control kinematics to contrast with the maximum two-bladed performance and maximum PFR conditions already mentioned. These were (1) a case with close to optimal power output but lower amplitude than the maximum $\overline{C_P}$ case and (2) a suboptimal $\overline{C_P}$ condition, chosen to highlight detrimental performance and flow-field features. All four highlighted control kinematics can be found in table I along with the associated performance and PFR changes compared to that of a constant rotation speed operation. The relative time-averaged performance of each kinematic profile is also shown in Fig. 3. Reducing the amplitude of the intracycle motion from $A_\lambda = 0.62\lambda_0$ to $A_\lambda = 0.42\lambda_0$ between the "Max $\overline{C_P}$" and "Low A_λ optimal $\overline{C_P}$" conditions results in a drop in power output of only 3% while increasing PFR by 22%. This is due to the horizontal stratification of performance seen in Fig. 4, which indicates that changes in amplitude predominantly impact the magnitude of blade-level hydrodynamics but not their sign. Holding ϕ constant maintains similar dynamics, indicating it has the greatest impact on the timing and position of hydrodynamic phenomena. The highlighted suboptimal case purposely has the same amplitude as the low-amplitude optimal $\overline{C_P}$ case but a different phase offset.

C. 1-Bladed turbine performance

To allow the direct comparison of blade-level performance and hydrodynamics, a single-bladed turbine was also tested. This allows for direct linkages between phase-averaged performance and the mechanisms behind the observed performance improvement. It is acknowledged that single and double-bladed turbines are not equivalent due to differences in solidity, blade-wake interactions, and turbine induction. These influences result in a higher optimum tip speed ratio for a single turbine under constant speed control (see Fig. 3). However, we argue that the relative trends remain consistent between the single and double-bladed turbines under intracycle control at the same mean tip-speed ratio. Especially in the upstream half of the cycle,

TABLE I
KEY INTRACYCLE KINEMATICS AND ASSOCIATED PERFORMANCE METRICS

Control scheme	ϕ	A_λ	$\overline{C_P}$	$\overline{C_P}$ Gain	PFR	PFR Gain
Constant λ	—	—	0.341	—	0.137	—
Max $\overline{C_P}$ (★)	117°	$0.61\lambda_0$	0.390	14.4%	0.094	-31.3%
Low A_λ Opt. $\overline{C_P}$ (●)	117°	$0.399\lambda_0$	0.377	10.55%	0.115	-16.53%
Optimal PFR (■)	153°	$0.184\lambda_0$	0.352	3.145%	0.161	17.47%
Suboptimal $\overline{C_P}$ (▲)	171°	$0.399\lambda_0$	0.184	-46.01%	0.088	-35.97%

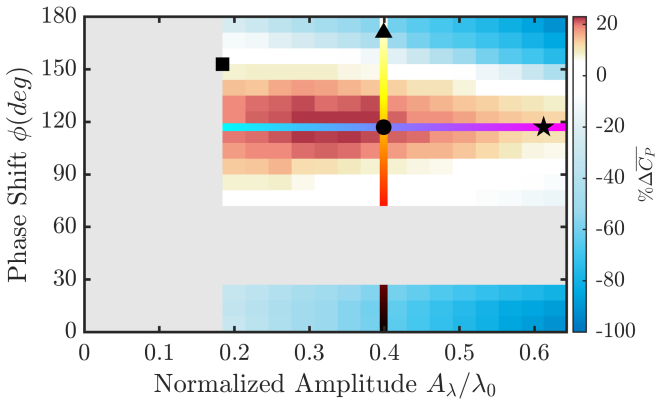

Fig. 6. Percent change in turbine $\overline{C_P}$ relative to constant speed (λ = 2) control condition for the one-bladed turbine. Vertical and horizontal lines correspond to the configurations explored with phase-averaged plots. The black symbols represent the kinematics of interest described in Fig. 4.

where the majority of power production occurs, and thus the single-bladed turbine phase-averaged performance profiles can be illustrative of the two-bladed turbine dynamics.

Single-bladed turbine performance, focusing on the region of expected improved efficiency, is shown in Fig. 6 for a mean tip-speed ratio of two and the same control scheme as the two-bladed turbine (where two accelerations occur per cycle). These results demonstrate a similar sensitivity to amplitude and phase offset as observed for the two-bladed turbine, albeit with a slightly broader range of phase offsets within which turbine performance could be augmented. Optimum single-bladed $\overline{C_P}$ is also seen to occur at lower A_λ values compared to the double-bladed turbine, close to the low-amplitude optimal $\overline{C_P}$ condition of the two-bladed turbine (purple circle). Maximum power output for the single-bladed turbine is seen to be 23% above that of the single-bladed turbine under constant speed control at the same tip-speed ratio. Note that we do not explore PFR for the one-bladed turbine as it is not currently possible to subtract the influence of the supports and accelerations, as noted previously.

Plotting a range of phase-averaged performance profiles with one fixed intracycle control parameter further highlights the performance impacts of each control variable. We explore the influences of phase offset and amplitude along the vertical and horizontal lines shown in Fig. 6. The influence of increasing amplitude is illustrated in Fig. 7a for ϕ = 115°. Peak efficiency increases with amplitude and occurs slightly later in the rotation and later in time. At very high $A_\lambda = 0.64\lambda_0$, more small-scale fluctuations are observed, likely due to increased fitting error of the controller at this amplitude; however, it is clear that excursions in power are also increasing in the downstream region, independent of these additional oscillations. This may be due to the second blade acceleration in the downstream region working to delay flow reattachment for high amplitudes. Fig. 7b, shows C_P as a function of time normalized by the period of a revolution, τ. As A_λ increases, the height of the performance peak continues to increase while the width of the C_P curve decreases, explaining the presence of an optimum amplitude that was not apparent when the performance was plotted as a function of the azimuthal position.

Significantly more variable phase-averaged performance profiles are observed in Fig. 8a for fixed A_λ = 0.42 with varying ϕ. When ϕ = 45 - 99° small and early peaks suggest flow separation and a dynamic stall vortex that is shed prematurely. For values of ϕ = 117 - 144° the best performance is observed, with the highest and widest C_P peaks. However, as ϕ increases further, the performance peak reduces, likely due to out-of-sync torque and angular velocity peaks identified in prior work [5]. In each case, it also appears that detrimental performance in the upstream blade path tends to be associated with detrimental torque in the downstream region.

Phase-averaged performance results are shown for the one-bladed turbine operating under the two-bladed control scheme for four highlighted control kinematics in Fig. 9. The max $\overline{C_P}$ case has been excluded since the high turbine forces prevented PIV capture using the cantilevered configuration. The previously highlighted kinematics of interest are outlined in Table I. We investigate these four cases to highlight ties between performance and kinematics as a function of position and time. Fig. 9a shows the phase-averaged power coefficients C_P, torque coefficients, C_Q, variation in rotation rate, and changes in nominal blade relative velocities and angles of attack. The low A_λ optimal C_P case displays a higher relative velocity than the other cases, which would enhance lift generation and perhaps aid the maintenance of flow attachment due to a higher local Reynolds number. In the downstream region, despite greater uncertainty in the angle of attack and blade-relative velocity, α_n and U_n profiles suggest that the optimal kinematics result in a faster reduction in α_n and thus faster flow recovery post-stall than the constant speed case. This is supported by the diminished blade wake observed in the PIV flow-fields to be discussed in the following section (Fig. 10). The

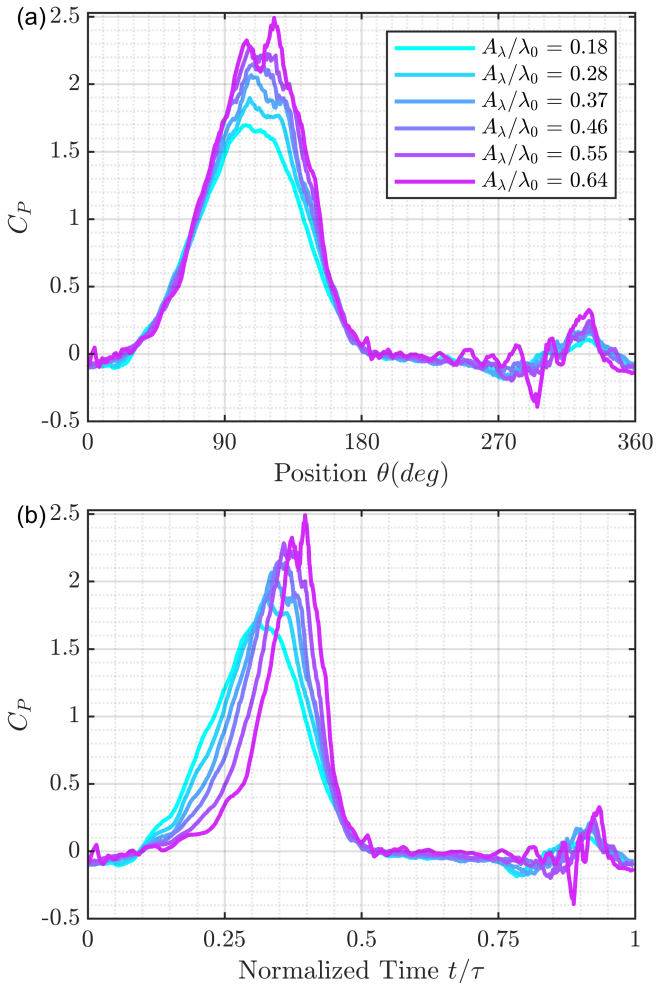

Fig. 7. Phase averaged support subtracted performance C_P as a function of position (a) and time (b), for fixed optimal phase shift, ϕ = 117° and varying A_λ.

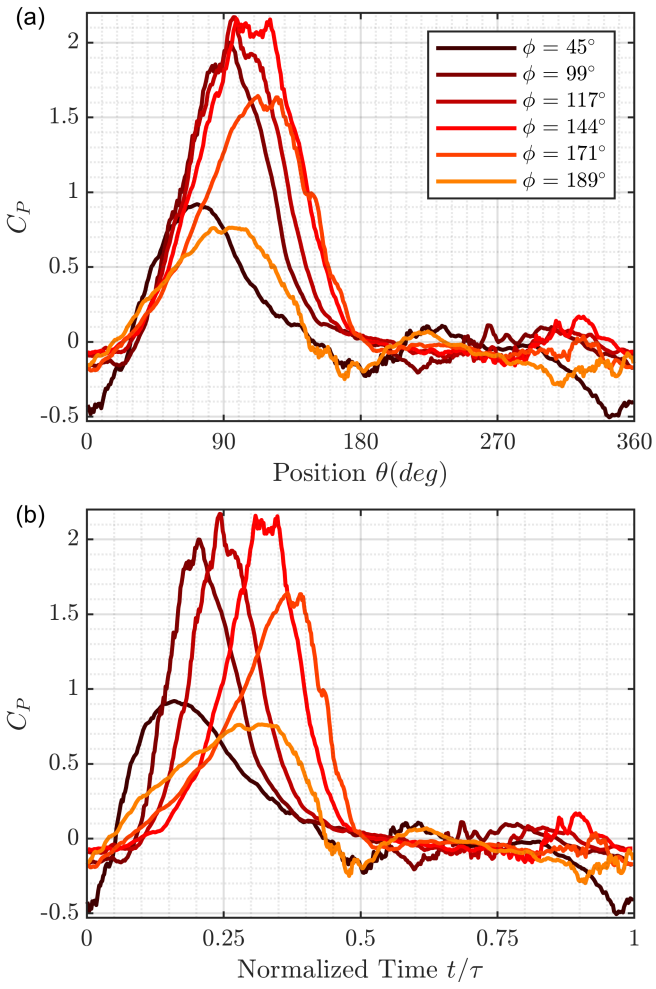

Fig. 8. Phase averaged support subtracted performance as a function of position (a) and time (b), for A_λ = 0.40λ_0 and varying ϕ.

suboptimal case shows a higher and early spike in α_n, which would trigger an earlier and deeper dynamic stall, resulting in the early drop in power seen in Fig. 9a.

Finally, we explore the optimal PFR case, which has significant similarities to the constant speed case. This is not altogether unexpected due to the smaller A_λ value. Smoother α_n and nominal velocity profiles near peak performance suggest that these kinematics flatten excursions in force, leading to improved PFR. This is shown in the efficiency plot as a function of normalized time (Fig. 9b), where the PFR case shows a decrease in peak amplitude, but the width of the power-producing region is the largest.

D. 1-Bladed PIV

PIV flow-fields were acquired for the one-bladed turbine under three intracycle conditions and one constant speed case. These were the conditions of Table I but without the case corresponding to true maximum $\overline{C_P}$ of the two-bladed turbine. This case was excluded in favor of the lower amplitude optimum case to diminish the loading of the cantilevered PIV rotor assembly. Similarly, the optimum one-bladed kinematic was seen to occur at lower amplitudes, and thus, the low-amplitude optimum case is of greater interest. Hydrodynamics in the power-producing portion of the cycle are thought to be similar between the two cases based on the analysis of Fig. 7 and 8.

Near-blade flow-fields are shown in Fig. 10, highlighting key phases of the cycle in the power-producing portion of the rotation and downstream flow recovery. Red and blue vorticity represent clockwise and counterclockwise rotations, respectively. Under constant speed control, the leading edge vortex is seen to form along the inside of the blade, resulting in a maximum torque that peaks early in the cycle (around 100°), see Fig. 9a before shedding well before the blade passes into the downstream sweep. In contrast, kinematics for optimal power generation holds the vorticity closer to the blade for longer, with the vortex shedding much closer to the upstream/downstream transition. This would appear to be the benefit of holding the angle of attack approximately constant after exceeding the static stall angle, resulting in prolonged lift and torque generation. The shed vortex is also smaller, potentially leading to faster flow recovery.

In contrast, the suboptimal kinematics produce a much larger and earlier formation of the dynamic stall vortex, which follows the blade through the power-producing phases, suggesting a prolonged region of

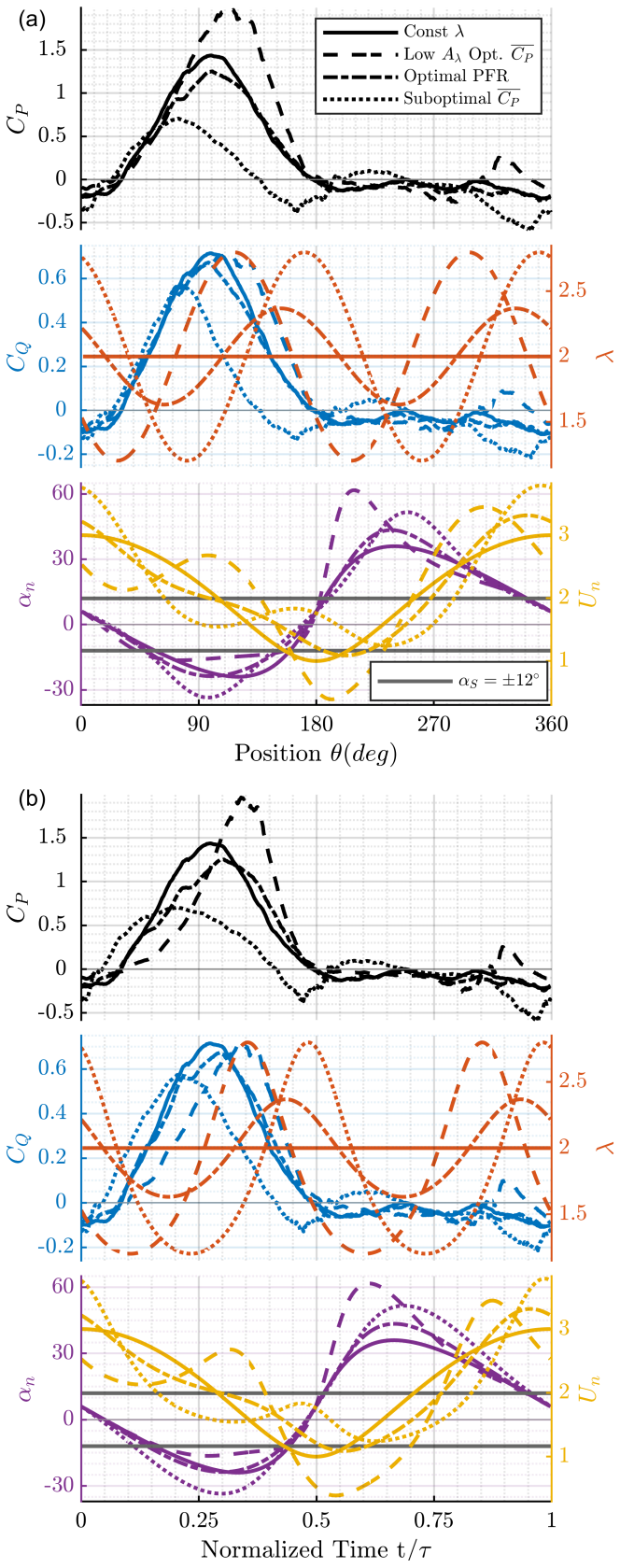

Fig. 9. Phase average comparison of single blade power coefficient, torque coefficient (aligned with control λ), and nominal velocity and AoA, for constant speed control λ = 2 and three key intracycle kinematics documented above, and differentiated by line type, as a function of position (a) and time (b). The static stall angle, α_s, of ±12 - 15° seen at similar Reynolds numbers [12], [13], is also indicated.

low lift. Interestingly, a secondary dynamic stall vortex appears to shed from the blade around 270°, indicating that some lift generation occurs in phases just before this, in line with the phase-averaged performance results. Later in the cycle, 304 - 329°, discrete clockwise and counterclockwise vortices are seen along the bladed, which reduces lift and increases drag, resulting in the notable negative performance shown in Fig. 9a that was not observed in the other cases.

PFR kinematics produce subtly different flow-fields from those with constant rotation rates, consistent with the performance results. The stall vortex is slightly larger and appears to develop and shed slightly earlier and more diffusely than observed for constant speed control. Flow recovery also appears similar. These observations are consistent with the hypothesis that the PFR kinematics are smoothing out excursions in the angle of attack and blade-relative velocity normally associated with intracycle kinematics, leading to smaller excursions in blade forcing. This is confirmed in the efficiency plot as a function of normalized time (Fig. 9b), where the PFR case shows a decrease in peak efficiency, but the width of the power-producing region is the largest.

IV. Conclusion

The sensitivity of sinusoidal intracycle control of cross-flow turbines to changes in amplitude and phase was experimentally explored to broaden understanding of the optimization opportunities for power/efficiency and maximum loading. Complex interactions between performance and changes to in-rotor hydrodynamics were studied. Both single and double-bladed turbines were operated at a mean tip-speed ratio of two, corresponding to the optimum time-averaged performance of the two-bladed design under constant speed control. One-bladed data were acquired to explore variations in the phase-averaged performance of the blade, which were taken as informative of the two-bladed turbine despite differences in solidity, induction, and optimum mean tip-speed ratio.

It was found that two-bladed performance could be increased by up to 14.4% compared to the same turbine under constant speed control at the same tip-speed ratio. Performance increases could be consistently obtained within a narrow band of phase offsets (ϕ = 90 - 140°) and continuously increased with amplitude up to very high amplitudes ($A_\lambda = 0.64\lambda_0$) for the two-bladed turbine, at which point the ability of the controller to track the specified intracycle control profile degraded. Optimum control inputs for the intracycle turbine were ϕ = 117° and $A_\lambda = 0.61\lambda_0$ corresponding closely to the kinematics found by Strom *et al.* and Dave *et al.* for a similar turbine at comparable Reynolds numbers [5], [8]. Augmentation, compared to constant speed control was lower than that observed in earlier studies. This may partially be due to the subtraction of support parasitic drag in this study, different blade mounting structures, and slight differences in experimental non-dimensional parameters. Efficiency augmentation calculations are also highly sensitive to small changes in time-averaged constant-speed $\overline{C_P}$.

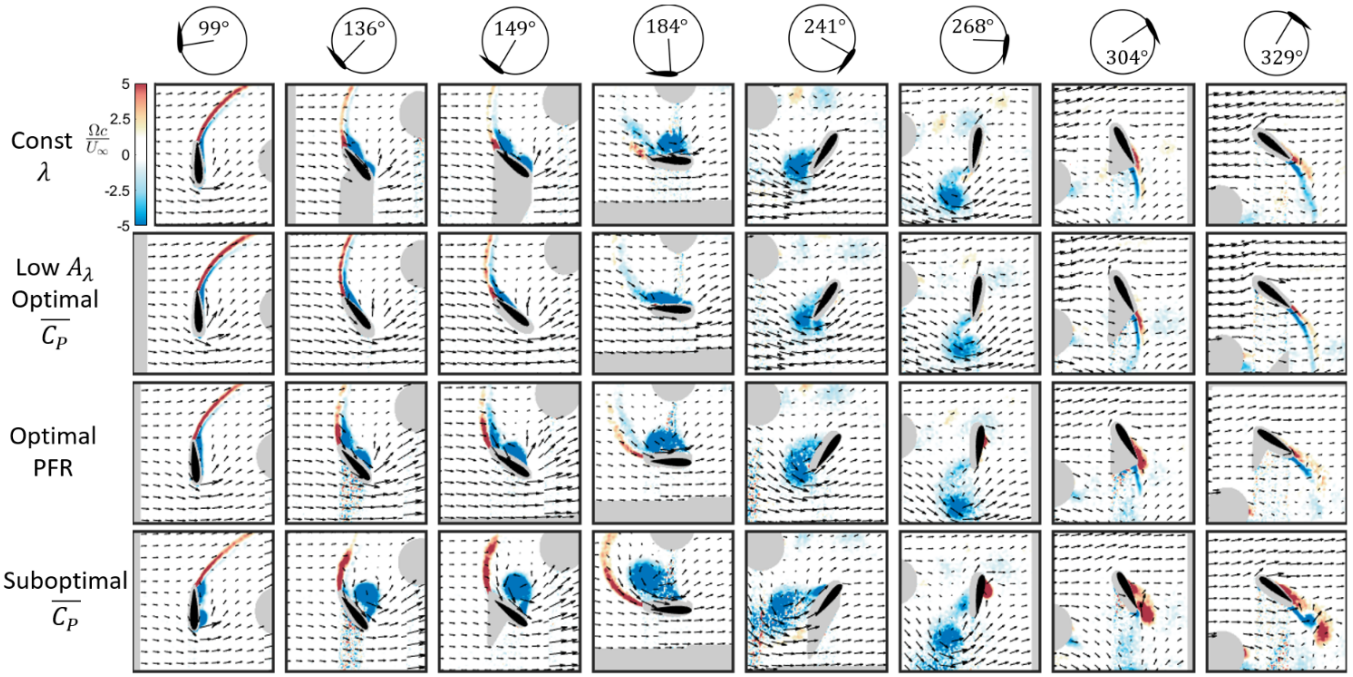

Fig. 10. Normalized PIV vorticity fields for a 1-bladed turbine at phases where the largest differences are apparent. Note that the velocity vectors are down-sampled by a factor of 15 from the full field and are in the turbine reference frame. Red and blue indicate clockwise and counterclockwise rotation, respectively. Masked regions (shadows or occlusions) are shown in grey.

The one-bladed turbine operating under the same control parameters as the two-bladed configuration, showed similar trends, however, the range of optimum phases was slightly wider (90 - 150°) while the optimum amplitude was lower than that observed for the two-bladed turbine ($A_\lambda = 0.34\lambda_0$). Overall, $\overline{C_P}$ could be increased by 23% relative to constant speed operation. As amplitude was increased, the upstream power-producing phase-averaged performance peak was observed to increase but also occur for less time, explaining the appearance of an optimum intracycle control amplitude for the one-bladed configuration. Consistent with earlier studies, power optimization involves aligning the maximum rotation rate and power production in the upstream power-producing stroke. The phase offset of the intracycle control scheme drives this alignment, hence the higher sensitivity of overall performance to this parameter.

Explorations of the nominal angle of attack and blade relative velocity (α_n and U_n, respectively) provide further insights into the sources of different intracyle performance. Under optimal efficiency conditions, the angle of attack increases at a similar rate to the other highlighted cases, however, once the static stall angle was exceeded, it remained almost constant until the shedding of the dynamics stall vortex. At the same time, blade-relative velocities remain higher for longer. Both of these trends should increase lift and prolong power extraction. Analysis of in-rotor flow-fields supports this conclusion, with a smaller and delayed dynamic stall vortex for optimal intracycle control, compared to the constant speed case. Despite high uncertainty in the nominal angles of attack and velocities in the downstream region, optimal efficiency kinematics also appear to help manage the post-stall flow recovery with a rapid drop in the angle of attack between 270 - 360°. In-rotor flow-fields corroborate this conclusion.

Inspecting suboptimal kinematic profiles further underscores the conditions needed for beneficial performance. Suboptimal kinematics appear to promote increased angles of attack early in the cycle, lower blade-relative velocities at the phases of peak lift, and the formation of a very strong dynamic stall vortex that sheds early in the cycle. When the intracycle phase shift was poorly chosen, secondary stall events are also prominent in the downstream blade sweep. It is clear the dynamic stall location and magnitude, as well as the aftermath, are closely tied to the torque peaks presented in the phase-averaged curves.

The maximum forces experienced by the rotor can often dictate turbine structural design, and so we explored the variation of average power to maximum in-plane forces (denoted PFR) throughout the intracycle parameter space. It is revealed that an optimum could be found whereby PFR could be increased by 17.5% through a 12% reduction of the peak loading while still slightly increasing power output in a two-bladed turbine ($\phi = 153°$ and $A_\lambda = 0.18\lambda_0$). When optimizing for PFR, both control parameters show a narrower beneficial range than observed for $\overline{C_P}$ optimization. The phase-averaged performance of a one-bladed turbine shows a slight offset between the torque peak and the max $\lambda(\theta)$ for the optimal PFR case, which appears to widen the power-producing region of the phase-averaged C_P as well as decrease the peak value. While optimum PFR performance profiles are only subtly different from those under constant rotation speeds, they were observed to smooth the projected nominal angle of attack and blade-relative velocity

profiles, which is thought to be the primary reason for reduced maximum loads. In-rotor flow-fields under optimal PFR control show dynamic stall vortex formation slightly earlier than in the constant speed case but a more diffuse vortex shed later in the cycle. Overall the flow-field is very similar to the constant speed case under this control strategy, as expected due to the smaller intracycle amplitude employed. By uncovering the intricacies of flow-fields and performance sensitivity of the intracycle control space, this work provides a stepping stone towards more adaptable and efficient control methods to achieve a diverse range of objectives.

ACKNOWLEDGEMENT

The authors would like to gratefully acknowledge the assistance of Aidan Hunt with initial configuration of the intracyle control scheme code. Also, to Jennifer Franck, Ph.D. and Mukul Dave, Ph.D. of the University of Wisconsin-Madison, for in-depth discussions on intracycle control dynamics.

REFERENCES

[1] J. O. Dabiri, "Potential order-of-magnitude enhancement of wind farm power density via counter-rotating vertical-axis wind turbine arrays," *Journal of renewable and sustainable energy*, vol. 3, no. 4, p. 043104, 2011.

[2] Z. Zhao, D. Wang, T. Wang, W. Shen, H. Liu, and M. Chen, "A review: Approaches for aerodynamic performance improvement of lift-type vertical axis wind turbine," *Sustainable Energy Technologies and Assessments*, vol. 49, p. 101789, 2022.

[3] A. Buchner, M. W. Lohry, L. Martinelli, J. Soria, and A. J. Smits, "Dynamic stall in vertical axis wind turbines: comparing experiments and computations," *Journal of Wind Engineering and Industrial Aerodynamics*, vol. 146, pp. 163–171, 2015.

[4] A. Choudhry, M. Arjomandi, and R. Kelso, "Methods to control dynamic stall for wind turbine applications," *Renewable energy*, vol. 86, pp. 26–37, 2016.

[5] B. Strom, S. L. Brunton, and B. Polagye, "Intracycle angular velocity control of cross-flow turbines," *Nature Energy*, vol. 2, no. 8, pp. 1–9, 2017.

[6] M. Dave, B. Strom, A. Snortland, O. Williams, B. Polagye, and J. A. Franck, "Simulations of intracycle angular velocity control for a crossflow turbine," *AIAA Journal*, vol. 59, no. 3, pp. 812–824, 2021.

[7] B. Polagye, B. Strom, H. Ross, D. Forbush, and R. J. Cavagnaro, "Comparison of cross-flow turbine performance under torque-regulated and speed-regulated control," *Journal of Renewable and Sustainable Energy*, vol. 11, no. 4, p. 044501, 2019.

[8] M. Dave and J. A. Franck, "Analysis of dynamic stall development on a cross-flow turbine blade with modal decomposition," *arXiv preprint arXiv:2301.07610*, 2023.

[9] A. Snortland, B. Polagye, and O. Williams, "Influence of near-blade hydrodynamics on cross-flow turbine performance," in *Proceedings of the 13th European Wave and Tidal Energy Conference*, 2019, pp. 1–9.

[10] P. Bachant, M. Wosnik, B. Gunawan, and V. S. Neary, "Experimental study of a reference model vertical-axis cross-flow turbine," *PloS one*, vol. 11, no. 9, p. e0163799, 2016.

[11] B. Strom, N. Johnson, and B. Polagye, "Impact of blade mounting structures on cross-flow turbine performance," *Journal of Renewable and Sustainable Energy*, vol. 10, no. 3, p. 034504, 2018.

[12] W. Timmer, "Two-dimensional low-reynolds number wind tunnel results for airfoil naca 0018," *Wind engineering*, vol. 32, no. 6, pp. 525–537, 2008.

[13] A. Bianchini, F. Balduzzi, J. M. Rainbird, J. Peiro, J. M. R. Graham, G. Ferrara, and L. Ferrari, "An experimental and numerical assessment of airfoil polars for use in darrieus wind turbines—part i: flow curvature effects," *Journal of Engineering for Gas Turbines and Power*, vol. 138, no. 3, 2016.